

MIT Open Access Articles

Domain-wall structure in thin films with perpendicular anisotropy: Magnetic force microscopy and polarized neutron reflectometry study

The MIT Faculty has made this article openly available. **Please share** how this access benefits you. Your story matters.

Citation: Navas, David, Carolina Redondo, Giovanni A. Badini Confalonieri, Francisco Batallan, Anton Devishvili, Oscar Iglesias-Freire, Agustina Asenjo, Caroline A. Ross, and Boris P. Toperverg. "Domain-Wall Structure in Thin Films with Perpendicular Anisotropy: Magnetic Force Microscopy and Polarized Neutron Reflectometry Study." Phys. Rev. B 90, no. 5 (August 2014). © 2014 American Physical Society

As Published: <http://dx.doi.org/10.1103/PhysRevB.90.054425>

Publisher: American Physical Society

Persistent URL: <http://hdl.handle.net/1721.1/89198>

Version: Final published version: final published article, as it appeared in a journal, conference proceedings, or other formally published context

Terms of Use: Article is made available in accordance with the publisher's policy and may be subject to US copyright law. Please refer to the publisher's site for terms of use.



Domain-wall structure in thin films with perpendicular anisotropy: Magnetic force microscopy and polarized neutron reflectometry study

David Navas,^{1,2,*} Carolina Redondo,³ Giovanni A. Badini Confalonieri,⁴ Francisco Batallan,⁴ Anton Devishvili,⁵ Óscar Iglesias-Freire,⁴ Agustina Asenjo,⁴ Caroline A. Ross,¹ and Boris P. Toperverg^{5,6}

¹*Materials Science and Engineering Department, Massachusetts Institute of Technology, Cambridge, Massachusetts 02139, USA*

²*Instituto de Física dos Materiais da Universidade do Porto – Instituto de Nanotecnologia and Departamento Física e Astronomia, Univ. Porto, 4169-007 Porto, Portugal*

³*Departamento de Química-Física, Universidad del País Vasco, 48940 Leioa, Vizcaya, Spain*

⁴*Instituto de Ciencia de Materiales de Madrid, Centro Superior de Investigaciones Científicas, Cantoblanco, 28049 Madrid, Spain*

⁵*Department of Physics, Ruhr-Universität Bochum, D-44780 Bochum, Germany*

⁶*Petersburg Nuclear Physics Institute, 188300 Gatchina, Russia*

(Received 9 May 2014; revised manuscript received 4 August 2014; published 28 August 2014)

Ferromagnetic domain patterns and three-dimensional domain-wall configurations in thin CoCrPt films with perpendicular magnetic anisotropy were studied in detail by combining magnetic force microscopy and polarized neutron reflectometry with micromagnetic simulations. With the first method, lateral dimension of domains with alternative magnetization directions normal to the surface and separated by domain walls in 20-nm-thick CoCrPt films were determined in good agreement with micromagnetic simulations. Quantitative analysis of data on reflectometry shows that domain walls consist of a Bloch wall in the center of the thin film, which is gradually transformed into a pair of Néel caps at the surfaces. The width and in-depth thickness of the Bloch wall element, transition region, and Néel caps are found consistent with micromagnetic calculations. A complex structure of domain walls serves to compromise a competition between exchange interactions, keeping spins parallel, magnetic anisotropy orienting magnetization normal to the surface, and demagnetizing fields, promoting in-plane magnetization. It is shown that the result of such competition strongly depends on the film thickness, and in the thinner CoCrPt film (10 nm thick), simple Bloch walls separate domains. Their lateral dimensions estimated from neutron scattering experiments agree with micromagnetic simulations.

DOI: [10.1103/PhysRevB.90.054425](https://doi.org/10.1103/PhysRevB.90.054425)

PACS number(s): 75.60.Ch, 75.25.-j, 75.30.Gw, 75.70.Ak

I. INTRODUCTION

Thin film materials with perpendicular magnetic anisotropy have been widely studied for perpendicular magnetic recording media [1,2] and patterned magnetic media [3,4]. They are also increasingly important in new devices based on the movement of domain walls (DWs) for data storage [5] and logic applications [6,7]. The aim is to control the DW motion using magnetic fields or spin-polarized currents. This requires highly efficient current-driven DW propagation, with high velocity under low current, combined with stability of the DW at a pinning site against thermal fluctuations. Materials with in-plane anisotropy, such as permalloy (NiFe), suffer from wide (>50 nm) DWs with low mobility [8,9], complex magnetization configurations, and large depinning current density, leading to undesirable Joule heating effects [9–11]. Thin films with perpendicular anisotropy [12–15] demonstrate several advantages over systems with in-plane anisotropy, such as narrow DWs with a simpler and more rigid DW structure, higher nonadiabatic effects leading to lower critical current densities and high DW velocities, and high thermal stability [16–18].

The response of DWs to magnetic fields and/or electric currents depends on the micromagnetic structure [19,20], and it is therefore important to fully characterize the DW morphology. The advent of high-resolution imaging techniques has opened up the possibility to image the wall position, and even the spin structure, on the nanoscale. DWs in magnetic films with

in-plane magnetization have been well characterized by several techniques, including magnetic force microscopy (MFM) [21], scanning electron microscopy with spin polarization analysis (SEMPA) [22], or x-ray photoemission electron microscopy (X-PEEM) [23]. DWs in films with perpendicular anisotropy are narrower (e.g., with widths of a few tens of nanometers), making analysis more challenging. X-ray magnetic circular dichroism (XMCD) gave an average domain-wall width of $\approx(30 \pm 10)$ nm in a Co/Pt multilayer with perpendicular magnetic anisotropy [24], and Lorentz microscopy gave a mean domain-wall width of ≈ 20 nm in FePd thin films [25]. Magnetic coupling led to a transformation from a classical Bloch wall, observed in single layers, to a Néel wall in Au/Co multilayers according to MFM and ballistic electron emission microscopies (BEEMs) [26]. In Co (0001), a domain-wall width as thin as ≈ 2 nm and closure domains at the surface of the sample were determined by spin-polarized scanning tunneling microscopy (Sp-STM) [27].

Therefore, the structure of DWs in films with perpendicular anisotropy is not simply a classical Bloch or Néel wall. In 1946, Kittel [28] predicted that the DW consisted of a Bloch wall in the center of the thin film with two Néel caps at the surfaces providing flux closure [29]. In 1999, Dürr *et al* [30] demonstrated the existence of 12.5-nm-thick closure domains with in-plane magnetization in a 40-nm-thick FePd film with perpendicular anisotropy using circular dichroism in x-ray-resonant magnetic scattering (CDXRMS). In this work, we have studied the DW structure with the use of polarized neutron reflectivity (PNR) measurements. In contrast with other magnetic measurement techniques which

*Corresponding author: davidnavasotero@gmail.com

provide volume-averaged information, PNR gives depth and lateral resolution for both the nuclear and the magnetic density distribution in the sample [31–33], allowing determination of the magnetization amplitude and direction in each layer, even when the magnetic layer is buried in a multilayer stack. Although PNR is only sensitive to in-plane magnetization [34], we will show that the domain-wall structure in materials with perpendicular anisotropy can be determined. Thin films of CoCrPt, an alloy which has received significant attention for perpendicular magnetic recording media [35,36], were studied. The anisotropy was oriented perpendicular to the film plane by growing the Co grains epitaxially on a Ti underlayer so the *c* axis was oriented out of plane [37,38].

The paper is organized as follows: in Sec. II, sample preparation details and methods employed are described; in Sec. III, the experimental and modeled data are reported and discussed, while Sec. IV highlights main results of the study. More details about the PNR analysis data treatment was added as an Appendix.

II. EXPERIMENTAL METHODS

A 5 nm Ti seed layer, a 10- or 20-nm-thick Co 66 at.%/Cr 22 at.%/Pt 12 at. % (CoCrPt) film, and a 3 nm Ti capping layer were deposited sequentially on (100) Si wafers with native oxide by RF sputtering at room temperature. The Ar (99.999% pure) sputtering gas pressure was 0.2 mTorr, with a base pressure below 2×10^{-8} Torr, and the RF power was 300 W for 5-cm-diameter targets [39]. The deposition rates were 1.9 Å/s for CoCrPt and 0.8 Å/s for Ti.

In the sputtering system, the thickness of the deposited layer was homogeneous over the central area ($\approx 2 \times 2$ cm²) of the sample but was reduced at larger radii. The hysteresis loops and the magnetic force microscopy images used samples with areas of 5×5 mm² cut from the center of the sample, where the layer thicknesses matched the nominal thickness values. However, polarized neutron measurements require larger areas, and samples were measured with areas as large as 3×3 cm². The average film thickness of the large samples is less than the nominal thickness, with a reduction of $\approx 15\%$.

Room temperature magnetic characterization was performed by measuring the hysteresis loops in a vibrating sample magnetometer (VSM, ADE model 1660). The ferromagnetic domain configurations were obtained using a magnetic force microscope (Veeco/Digital Instruments Nanoscope IIIa) with low moment Veeco tips. Two different states were studied: (1) After an out-of-plane ac demagnetizing process in which the sample was first saturated with an out-of-plane field of +10 kOe, then alternating positive and negative out-of-plane fields were applied where each step was 0.9 times that of the previous one; and (2) at remanence after in-plane saturation with +10 kOe.

Polarized neutron scattering experiments were carried out with the SuperADAM reflectometer [40] at the Institut Laue-Langevin, Grenoble (France). The measurements were performed with fixed neutron wavelengths of $\lambda = 0.441$ nm, and the polarization efficiency was around 95%. The external magnetic field (up to 7 kOe) was applied in-plane, parallel to the neutron polarization and perpendicular to the scattering plane. For specular reflectivity measurements, non-spin-flip

(NSF) reflectivities as well as neutrons with flipped polarization after reflection were analyzed.

Finally, micromagnetic simulations were performed using the National Institute of Standards and Technology (NIST) object-oriented micromagnetic framework (OOMMF) code [41]. The cell sizes and material parameters are described below, and the damping parameter was taken as 0.5 to ensure rapid convergence.

III. RESULTS AND DISCUSSION

The x-ray diffractometry pattern [inset in Fig. 1(b)] shows that the 20-nm-thick CoCrPt layer crystallized in a hexagonal close-packed phase. The well defined peaks correspond to Si (200) (not shown) and CoCrPt (0002) at $2\theta \approx 43.74^\circ$, indicating a (0001) texture [42–44]. Scherer’s equation gives a coherence length of ≈ 14 nm, similar to the grain size obtained by transmission electron microscopy in previous publications [36,45].

Both magnetic measurements (Fig. 1) and x-ray diffractometry (XRD) indicate that the crystallographic *c* axis and the easy magnetization axis were oriented out of plane [39,46,47]. Along the out-of-plane direction, the magnetization did not change until the external magnetic field reached the switching or “depinning field” (H_{Dp}). A sharp magnetization drop then

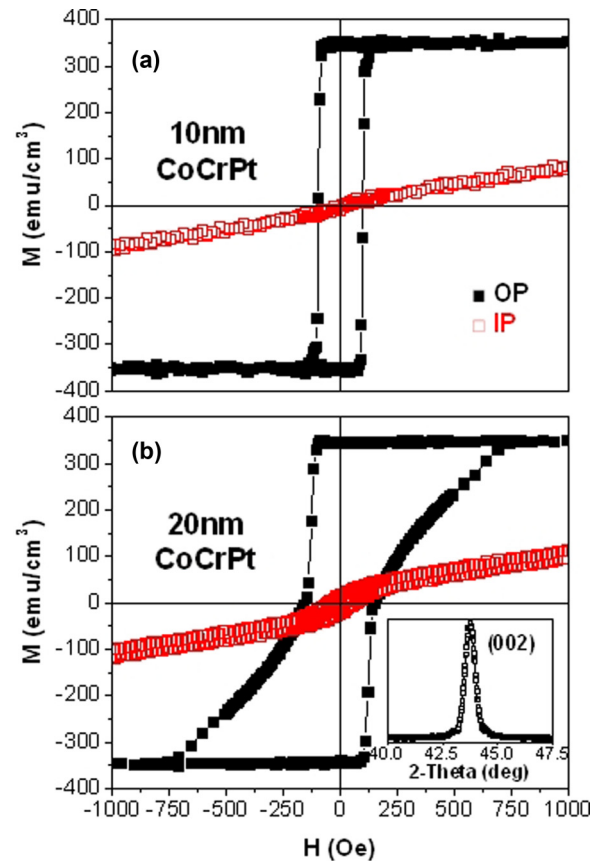


FIG. 1. (Color online) In-plane (□) and out-of-plane (■) hysteresis loops of (a) 10- and (b) 20-nm-thick CoCrPt films. The inset in (b) shows the one-dimensional XRD pattern of the 20-nm-thick CoCrPt thin film (□).

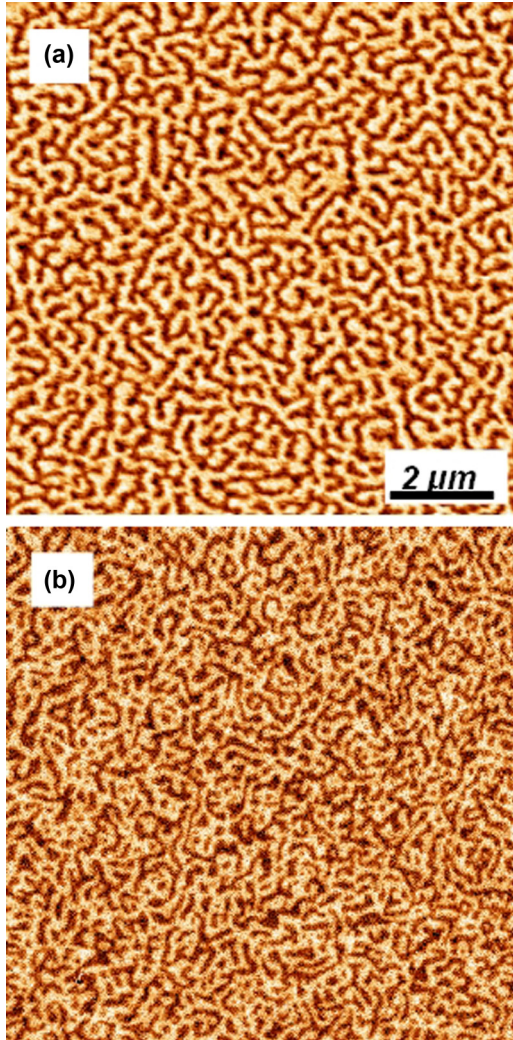


FIG. 2. (Color online) MFM images of 20-nm-thick CoCrPt film on a smooth substrate after an out-of-plane ac demagnetization process (a) and at remanence after in-plane saturation with +10 kOe (b). Both images were obtained at the same magnification.

occurred which was associated with expansion of reverse domains. While the hysteresis loop shape was almost square for the 10-nm-thick film [Fig. 1(a)], the 20-nm-thick film [Fig. 1(b)] showed a slow approach to saturation attributed to the existence of small bubble domains that are magnetostatically stabilized by the surrounding regions [48]. While the 20-nm-thick film had depinning and coercive fields of 97 and 154 Oe, respectively, the 10-nm-thick film showed smaller values of 82 and 98 Oe, respectively, and the remanence was close to 1 for both 10- and 20-nm-thick films. The in-plane loop, in contrast, was characteristic of a hard axis.

Figure 2(a) gives the MFM image of a 20-nm-thick CoCrPt thin film after an out-of-plane ac demagnetization. Stripe domains were present, typical of systems with perpendicular magnetic anisotropy. From the self-correlation transform of the MFM image [49], an estimation of the average domain size was $\approx(180 \pm 10)$ nm [50]. On the other hand, Fig. 2(b) shows the MFM images of the sample at remanence after in-plane saturation with +10 kOe. Again, a maze domain structure was

observed, with average domain size $\approx(140 \pm 10)$ nm. There was no detectable preferential in-plane directionality of the domains. The 10 nm film could not be imaged because the stray field of the MFM tip significantly modified the domain patterns.

The CoCrPt film consisted of polycrystalline grains in which the grains and the grain boundaries commonly differ in their composition and magnetic properties [51,52]. Although such microstructures can be modeled as Voronoi tessellations [53–55] or as regular hexagonal arrays [56,57], in this case grains with square [58] cross sections were considered, and modeling was carried out using the NIST OOMMF code [41]. Three-dimensional simulations, including two-dimensional periodic boundary conditions (PBCs) [59] neglecting thermal excitation effects (corresponding to zero temperature) [55,60], were carried out on both 10- and 20-nm-thick CoCrPt layers. The cell size was set to $5 \times 5 \times 2$ nm³, and areas of 1×1 μm² and 500×500 nm² were modeled. To better approximate the microstructure, the film was divided into rectangular crystalline “grains” of $10 \times 10 \times 20$ nm³, in which each grain had a random 7° deviation of its uniaxial anisotropy from the film normal [see Fig. 3(a)], based on x-ray diffraction measurements of the distribution of the crystallographic *c* axis [39,61]. From the hysteresis loops, a uniaxial out-of-plane anisotropy energy of $K_u \approx 1.225 \times 10^6$ ergs/cm³ was estimated, and the M_S was taken as 350 emu/cm³, in agreement with literature values [46].

Figure 3(b) shows the micromagnetic simulation of a 20-nm-thick CoCrPt film after ac demagnetization for an image size of 1×1 μm². Taking the exchange stiffness constant $A = 5 \times 10^{-7}$ ergs/cm [62] gave a ferromagnetic maze structure with domain sizes close to the 180 nm observed experimentally. Figure 3(d) shows the micromagnetic simulation of the same sample at remanence after in-plane saturation, which also produced a maze domain structure with a smaller average domain width consistent with experiment. Micromagnetic simulations of the 10-nm-thick CoCrPt layer also predicted a maze configuration at remanence after in-plane saturation [Fig. 3(e)]. A comparison between the in-plane hysteresis loops (□), the PNR data (▲), and the micromagnetic simulations (●) of the 20- and 10-nm-thick CoCrPt layers are shown in Figs. 3(f) and 3(g), respectively. Even assuming that our micromagnetic simulation did not consider several aspects, such as the model at 0 K, with PBCs, neglecting possible exchange-decoupling between grains due to grain-boundary segregation, etc., the micromagnetic hysteresis loops show a reasonable agreement with the experimental data obtained by VSM and PNR.

In order to study the domain-wall structure of the 20-nm-thick film, we focus on the different components of the magnetic moment (M_x , M_y , and M_z) of a DW, shown in Figs. 4(a)–4(c), respectively. The wall lies along *x*, with *z* the out-of-plane direction. The micromagnetic simulation confirms that the DW consisted of a Bloch wall at the midthickness of the film with two pseudo-Néel caps at the surfaces where the magnetic flux is partially closed within the film [29]. Schematic diagrams of the DW are shown in Figs. 4(d) and 4(e). In comparison, micromagnetic simulations of the 10-nm-thick CoCrPt layer [Fig. 3(e)] suggested that the DW had a pure Bloch character [Fig. 4(f)] without the Néel caps.

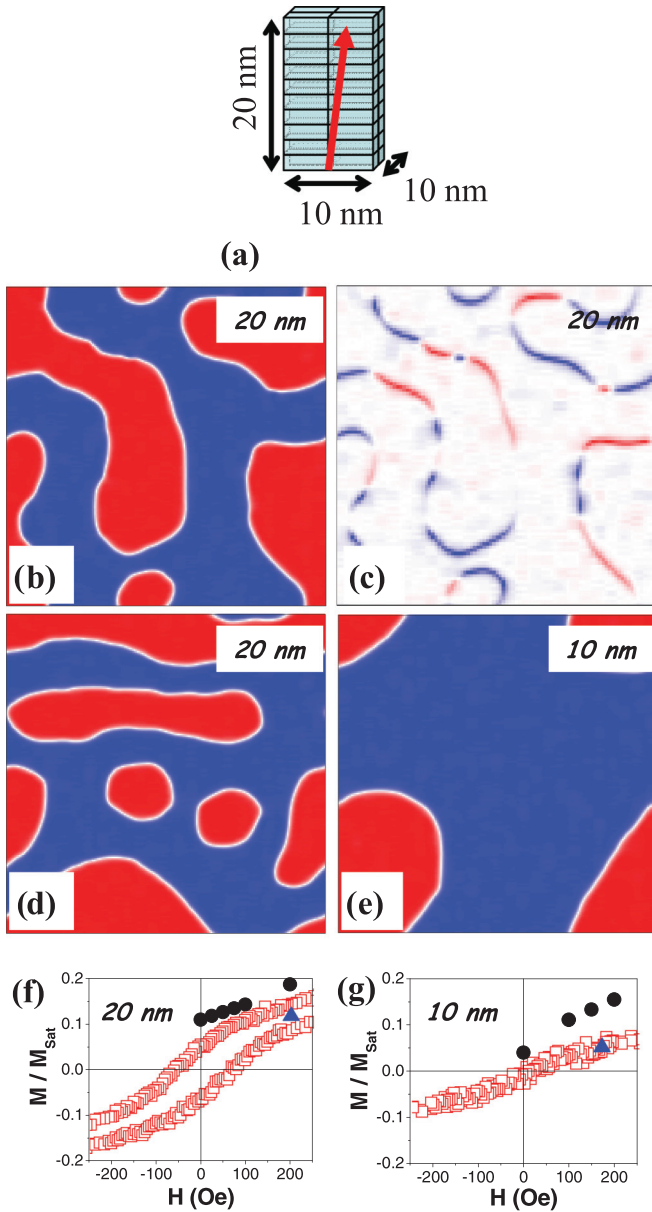


FIG. 3. (Color online) A CoCrPt rectangular crystalline grain of $10 \times 10 \times 20 \text{ nm}^3$ made of smaller cells of $5 \times 5 \times 2 \text{ nm}^3$. The c crystallographic axis (\uparrow) of each grain deviated by $\approx 7^\circ$ from the film normal. Top view of the micromagnetic simulations of a 20-nm-thick CoCrPt film with image sizes of $1 \times 1 \mu\text{m}^2$ (b, c) after out-of-plane ac demagnetization. (b) The out-of-plane component of the magnetic moment (M_z); (c) the component of the magnetic moment parallel to the external magnetic field or x axis (M_x). Top view of the micromagnetic simulations of a 20-nm-thick CoCrPt film with image sizes of $1 \times 1 \mu\text{m}^2$ at remanence (d) after in-plane saturation. (e) Top view of the micromagnetic simulations of a 10-nm-thick CoCrPt film with area of $1 \times 1 \mu\text{m}^2$ at remanence after in-plane saturation. (f, g) The in-plane VSM hysteresis loops (\square), the micromagnetic simulations (\bullet), and the PNR data (\blacktriangle) of the 20- and 10-nm-thick CoCrPt films, respectively. The red color shows the magnetic moment along the $+z$ axis (M_z), and blue shows the magnetic moment along the $-z$ axis (M_z) (b, d, and e). On the other hand, (c) the red color shows the magnetic moment along the $+x$ axis (M_x), and blue shows the magnetic moment along the $-x$ axis (M_x).

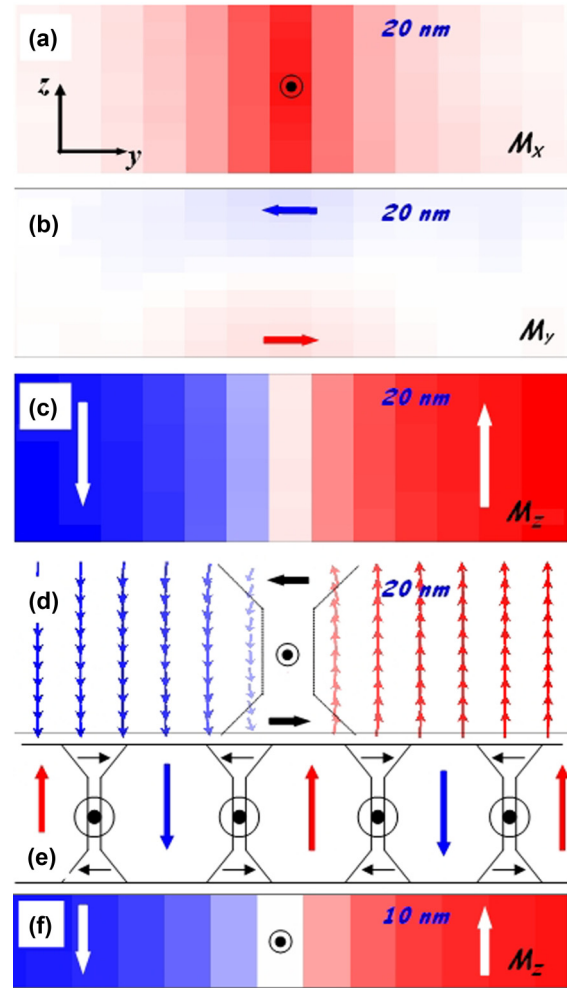


FIG. 4. (Color online) The components (a) M_x , (b) M_y , and (c) M_z of the magnetic moment in the yz plane of a DW oriented along x for a 20-nm-thick film. The red color shows the magnetic moment along the $+x$ axis in (a), $+y$ axis in (b), and $+z$ axis in (c), and blue shows the magnetic moment along the $-x$ axis in (a), $-y$ axis in (b), and $-z$ axis in (c). The inset in (a) shows the coordinate axes. A DW (d) and several DWs (e) formed by a Bloch wall in the center of the thin film with two Néel caps at the surfaces. (f) z component of the magnetic moment (M_z) of a DW in a 10-nm-thick CoCrPt film consisting of a Bloch wall. Red and blue colors show the magnetic moments along the $+z$ axis and $-z$ axis, respectively.

Polarized neutron reflectivity experiments were performed to study the magnetic configuration through the depth of the thin films. Two NSF, R^{++} and R^{--} , as well as two spin-flip (SF), R^{+-} and R^{-+} , reflectivity curves were recorded for both samples subjected to an external magnetic field up to 7 kOe applied within the sample surface. The NSF reflectivities probe the magnetization projection onto the in-plane magnetization direction, while the external field guiding the neutron polarization is applied in the same plane. SF reflectivities are sensitive to the in-plane magnetization components perpendicular to the magnetization direction. In order to analyze the experimental PNR data for thin films and multilayers, the theoretical reflectivity curves are usually calculated assuming a potential $V(z)$ depending on the coordinate z normal to the sample

surface. Then, the actual profile $V(z)$ is approximated by the histogram for which the reflection amplitudes can be found following the iterative routine called Parratt formalism.

The potential of each step in the histogram, representing a sublayer, is proportional to the sum of nuclear $Nb(z)$ and magnetic $Np(z)$ scattering length densities (SLDs) for positive neutron spin projection onto the magnetization direction. Alternatively, $V(z)$ is proportional to the difference of $Nb(z)$ and $Np(z)$. Then, a Parratt-type recursion formalism generalized for polarized neutron reflection [63] from a sequence of sublayers with arbitrary arrangement of layer magnetization vectors is applied to calculate the reflection amplitudes R^+ and R^- . After that, four NSF and SF reflection coefficients represented via bilinear combinations of amplitudes R^+ and R^- are averaged over directions of magnetization (see the Appendix). Then, in our PNR data treatment, all four reflectivities were simultaneously fitted to a theoretical model of the magnetization distribution across the film thickness and the sample surface by using an originally developed algorithm, known as a superiterative algorithm (see Refs. [34] and [63] for a detailed description), and a standard least squares routine, from which a set of structural and magnetic parameters were determined.

As the first step, the PNR analysis should be applied to the multilayered sample when it is saturated. From the fitting of the saturated experimental data, we are able to obtain several physical parameters of the sample such as the thicknesses, interfacial roughness, and both nuclear and magnetic SLDs of each layer. From the nuclear and magnetic SLDs, the corresponding chemical composition and magnetization of

each layer are determined, respectively. In order to achieve a good fitting process, we start the fitting using the layer thicknesses (obtained from other techniques such as atomic force microscopy), nuclear and magnetic SLDs (extracted from literature), and interface roughness of each layer as seed values, and keeping those parameters related with the experiment configuration fixed such as the neutron beam wavelength (4.4 Å), instrumental resolution, the number of experimental points supplied with corresponding error bars, etc.

Next, we can treat the PNR data of the sample in any other magnetic state. In this case, we fix all structural parameters independent of magnetic field (e.g., layer thicknesses and nuclear SLD of each layer, obtained from the saturated state analysis), and the magnetization behavior of each layer can be determined at different applied fields.

Finally, and in order to guarantee that the best fit has been achieved, we should check that the fitted data of each layer agree with the theoretical values and, by varying the step number in the magnetization profile histogram, we should reduce the statistical errors for each parameter as much as possible. Moreover, the reduced χ^2 parameter that is typically employed as a goodness-of-fit metric for iterative fitting of reflectivity data should be the smallest value in our least squares fitting routine. A reasonable χ^2 value, according to our standards, must range between 1 and 1.5. More details in PNR ideology and analysis are given in the Appendix.

The results for the 10- and 20-nm-thick CoCrPt films, measured both in saturation (7 kOe) and in a low field (≈ 200 Oe), are presented in Fig. 5. In saturation, one can

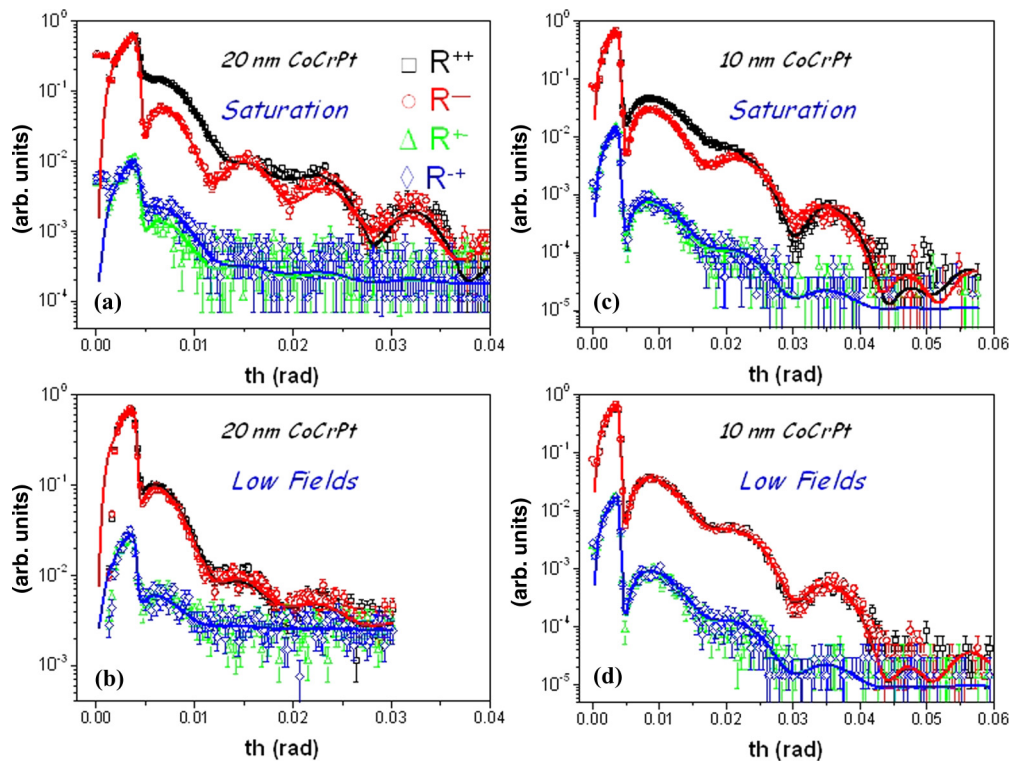


FIG. 5. (Color online) Polarized neutron experimental data (open symbols) and fit (lines) versus angle “th” from the (a, b) 20- and (c, d) 10-nm-thick CoCrPt films in (a, c) saturated and (b, d) low field states. R^{++} (\square and black line), R^{-} (\circ and red line), R^{+-} (\triangle and green line), and R^{-+} (\diamond and blue line).

clearly see the splitting between reflection curves R^{++} and R^{--} . This splitting is caused by the difference in SLDs $Nb + Np$ and $Nb - Np$ for alternative neutron spin projections onto the mean magnetization of the layers, with Nb and Np the nuclear and magnetic SLD, respectively. SF reflection, in principle, probes deviations of magnetization from the external field direction. For data obtained at saturation, the SF signal in Figs. 5(a) and 5(c) can be attributed entirely to the imperfect incident beam polarization (96.4%) and efficiency (95.3%) of the spin analysis. The tiny splitting of the NSF signals, which can be recognized at low fields in Fig. 5(b) and even in Fig. 5(d), can be attributed to small, but not negligible, in-plane magnetization components parallel to the external field.

Measurements in a saturating in-plane field of 7 kOe were used first to determine the basic sample parameters (i.e., average thicknesses, nuclear and magnetic scattering length densities, and interfacial roughness of the multilayer). They were reliably determined from the best fit of the PNR data to the theoretical model depicted in Figs. 5(a) and 5(c). The fitted ferromagnetic layer thicknesses were (8.0 ± 0.1) and (17.0 ± 0.1) nm for nominally 10- and 20-nm-thick CoCrPt layers, respectively. As expected, the thicknesses of the thin magnetic layers deviated appreciably from the nominal values of 10 and 20 nm in the 3×3 cm² samples due to the lower deposition rate at the edges of the sample.

Previous papers [42,44,64,65] have shown that when a CoCrPt film is grown on a Ti underlayer, an amorphous interlayer is formed, due to the large lattice mismatch and/or interdiffusion to form a Co-Ti amorphous alloy. PNR measurements indicated that the ferromagnetic material consisted of two regions: a polycrystalline layer of CoCrPt on top of a thin amorphous film. The polycrystalline CoCrPt layer thickness was (6.20 ± 0.06) and (15.18 ± 0.08) nm for nominally 10- and 20-nm-thick films, respectively, with an average nuclear SLD of $Nb = (3.09 \pm 0.02) \times 10^{-6} \text{ \AA}^{-2}$, close to the theoretical value of $Nb = 2.98 \times 10^{-6} \text{ \AA}^{-2}$. The PNR magnetization value is consistent with the values determined from the hysteresis loops and reported in literature ($M_S \approx 350 \text{ emu/cm}^3$) [46]. On the other hand, the CoCrPt/Ti amorphous layer showed an average thickness of (1.79 ± 0.06) nm in both samples, in agreement with the literature [42,44,64,65] and a nuclear SLD of $Nb = (1.78 \pm 0.07) \times 10^{-6} \text{ \AA}^{-2}$. Therefore, the interdiffusion of Ti, which has negative $Nb = -1.95 \times 10^{-6} \text{ \AA}^{-2}$, into the CoCrPt alloy is confirmed by the reduction of the nuclear SLD from $Nb = (3.09 \pm 0.02) \times 10^{-6} \text{ \AA}^{-2}$ for the CoCrPt layer to $Nb = (1.78 \pm 0.07) \times 10^{-6} \text{ \AA}^{-2}$ for the amorphous interlayer. Considering both CoCrPt and Ti nuclear SLDs, we estimate that the Ti concentration was $\approx 26\%$ inside the CoCrPt/Ti amorphous layer. From the magnetic point of view, the amorphous CoCrPt/Ti interlayer behaved as a nonmagnetic layer with a magnetic scattering length density of $Np = (0.00 \pm 0.09) \times 10^{-6} \text{ \AA}^{-2}$, also consistent with interdiffusion. Apart from this, the quality of the samples was rather good, and the roughness of the interfaces did not exceed 1 nm.

In order to determine the magnetization profile across the films at low field, further measurements were performed in $H \approx 200$ Oe (i.e., at the point where magnetization shows a linear dependence [see Fig. 1] and is substantially reduced with respect to that measured at 7 kOe). We expect

that the magnetization profile may be different in the true remanence state for, e.g. thin and thick films, as the latter shows a pronounced hysteresis, while in the former, linear field dependence passes through zero. Unfortunately, the configuration of the instrument used in the present experiment did not allow us to clarify this question, and 200 Oe was the minimum field required to keep neutrons highly polarized ($>95\%$). Figures 5(b) and 5(d) show that the splitting between NSF reflectivities, and hence the net magnetization of the sample, was appreciably reduced with respect to that in saturation [Figs. 5(a) and 5(c)]. This conclusion immediately follows from the disappearance of the spin splitting between reflectivity curves in the two bottom panels in Fig. 5. The low in-plane magnetization is expected from the out-of-plane anisotropy of the CoCrPt.

From the fit of the PNR data obtained in saturated and near-remanence states, it follows that the magnetic SLD of the CoCrPt 20-nm-thick layer decreased to an average value of $Np = (0.13 \pm 0.03) \times 10^{-6} \text{ \AA}^{-2}$, suggesting that $\approx 11.6\%$ of the CoCrPt magnetic moment remained aligned with the applied in-plane field guiding the neutron polarization [Figs. 6 and 7(a)]. However, the best fit with $\chi^2 = 1.36$ and minimal correlations between varied parameters was achieved with gradients of magnetic SLD across the CoCrPt layer, as illustrated in Fig. 6. At the same time, fit quality without gradient was found to be worse by a factor of two, failing to

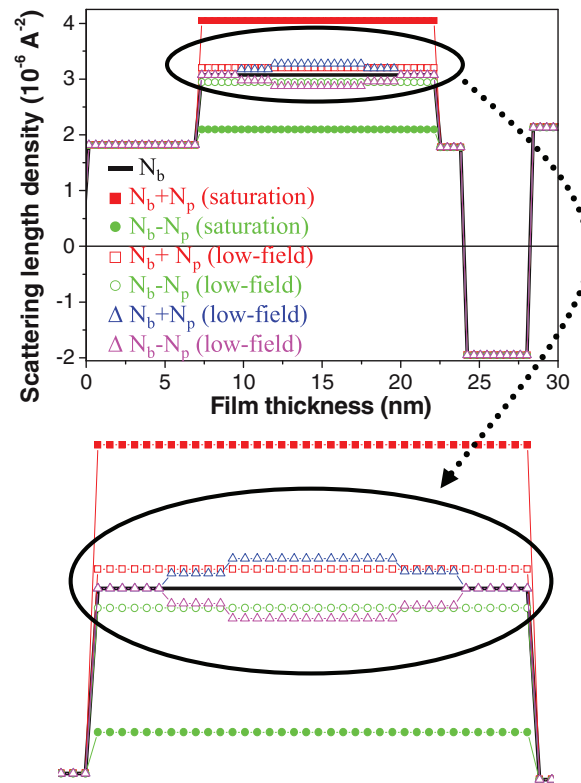


FIG. 6. (Color online) Nuclear SLD (—), (nuclear + magnetic) SLDs in saturation (■) and at low field without (□) and with (△) gradients of magnetic SLD, and (nuclear-magnetic) SLDs in saturation (●) and at low field without (○) and with (△) gradients of magnetic SLD of the 20-nm-thick CoCrPt film. On the bottom, a magnification of the SLDs, indicated by a circle, is shown.

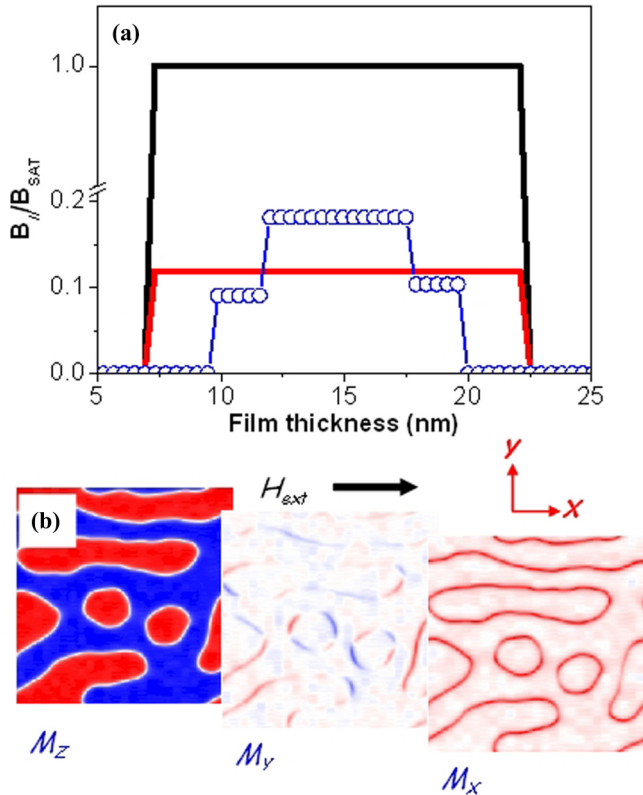


FIG. 7. (Color online) (a) Profile of the normalized in-plane magnetization in saturation (—) and at low field without (—) and with (○) gradients of magnetic SLD. (b) Components of the magnetic moment (M_x , M_y , and M_z) obtained from the micromagnetic simulation of the 20-nm-thick CoCrPt film at 200 Oe after in-plane saturation. The image size was $1 \times 1 \mu\text{m}^2$. The red color shows the magnetic moment along the $+z$ axis in M_z , $+y$ axis in M_y , and $+x$ axis in M_x , and blue shows the magnetic moment along $-z$ axis in M_z , $-y$ axis in M_y , and $-x$ axis in M_x .

satisfactorily describe oscillations in Fig. 5(b). A symmetric distribution of magnetization across the film thickness was observed with a gradual increase of the magnetic SLD from the surfaces [$Np = (0.0 \pm 0.1) \times 10^{-6} \text{ \AA}^{-2}$] to the center of the layer [$Np = (0.20 \pm 0.09) \times 10^{-6} \text{ \AA}^{-2}$]. This suggests a gradual decrease of in-plane magnetization of the CoCrPt layer from $\approx 18\%$ at the center of the layer down to $\approx 0\%$ of the saturation value at the surfaces [shown in Fig. 7(a)] and an intermediate region with in-plane magnetization of $\approx 10\%$.

A careful analysis of PNR data allows us not only to reconstruct the magnetization depth profile, but also to probe the lateral distribution of in-plane components of magnetization along the sample surface. This is possible due to the specific coherence properties of neutron radiation at grazing incidence and a specific procedure of lateral averaging applied in the PNR data treatment [34]. In fact, the SLD value reported above is the quantity averaged over the lateral projection of the neutron coherence ellipse, whose long axis is extended along the beam projection onto the surface over a distance up to $100 \mu\text{m}$. In contrast, the short axis of the ellipse is on the order of a few tens of nanometers. However, if magnetic domains in the near-remanence state form a maze pattern,

such as that shown in Fig. 2, then the coherence ellipse crosses a number of domains with alternating directions of magnetization perpendicular to the surface, as well as a number of DWs separating those domains. Note that the magnetization component normal to the surface, and hence the perpendicular domains, do not contribute to the PNR signal, and it is exclusively produced by the DWs. This fact was confirmed by the micromagnetic simulations of the 20-nm-thick CoCrPt film with an image size of $1 \times 1 \mu\text{m}^2$, where the components of the magnetic moment (M_x , M_y , and M_z) at 200 Oe (after in-plane saturation) are shown in Fig. 7(b). Therefore, the magnetic moment along the x axis (parallel to the external applied field) was mainly localized at the DWs.

The first clue to exclude the scenario that the magnetic domains could be separated by Néel walls was based on our CoCrPt micromagnetic simulations showing that domains with out-of-plane anisotropy are separated by a DW with a Bloch wall configuration at the center of the film and with Néel caps at the surfaces (Fig. 3). From the PNR data analysis, one can exclude the existence of extended Néel walls because their magnetic moments must be oriented in alternating directions in neighboring DWs in order to satisfy the continuity of the respective components of the magnetic flux (magnetic flux conservation law) [66]. Therefore, and in contradiction to our observations, the net magnetization due to Néel DWs should vanish after averaging over the coherence ellipsoid covering many of them. Even in the case of Néel walls that are far enough apart to avoid magnetostatic interactions, allowing the magnetic moments of neighboring walls to all point along the applied field direction, the wall widths should be constant along the film thickness, and a constant magnetic scattering length density (Np) would be expected with Np signal $\neq 0$ at the film surfaces. This scenario also contradicts our experimental observations, where the assumption about large distance between walls was not confirmed by MFM, with domain size $\approx (140 \pm 10) \text{ nm}$ and a gradual increase of the magnetic SLD from the surfaces to the center of the layer obtained from the PNR analysis. Therefore, we dismiss the formation of domain-wall configuration involving a Néel wall in the film center of the samples.

On the other hand, the Bloch DWs, by definition, possess an in-plane component of magnetic moment along the DW and may be oriented either parallel or antiparallel in neighboring Bloch walls. If the magnetization directions of the DWs are random, such as after a demagnetization process, the magnetic moment along the DW should be oriented antiparallel in neighboring Bloch walls [shown in Fig. 3(c)]. Then, and considering two neighboring walls, the magnetic moments of each wall should be pointed along the x axis (M_x) and the $-x$ axis ($-M_x$), respectively, and the mean value of magnetization is null, as is the magnetic SLD term.

However, our samples were studied after in-plane saturation. Micromagnetic simulations of the 20-nm-thick CoCrPt film at 200 Oe, and after in-plane saturation [Fig. 7(b)], show that the magnetic moment along the x axis and parallel to the externally applied field is mainly localized at the DWs. Moreover, the magnetic moments of all DWs have positive projections onto $+x$ axis (no walls were obtained with magnetic moments pointing along $-x$ axis). Therefore, if we consider two neighboring walls, the magnetic moments

of both walls are pointed mainly along the $+x$ axis (M_x), and the mean value of magnetization, as well as the magnetic SLD term, is not null.

In the case that two domains with out-of-plane magnetization would be separated by a pure Bloch wall, its width should be constant along the film thickness, and a constant magnetic scattering length density (Np) should be expected through the film thickness. However, the quantitative PNR analysis showed a gradual increase of the magnetic SLD from the surfaces [$Np = (0.0 \pm 0.1) \times 10^{-6} \text{ \AA}^{-2}$] to the center of the layer [$Np = (0.20 \pm 0.09) \times 10^{-6} \text{ \AA}^{-2}$]. This suggests a gradual decrease of in-plane magnetization of the CoCrPt layer parallel to the external field from the center of the layer to the surfaces, and a more complex structure of the DW is required.

Based on this approximate magnetization configuration, and considering that the mean contributions of both M_y and M_z are null in the PNR analysis, we will show that the behavior of the magnetization through the thickness of the nominally 20-nm-thick CoCrPt film, obtained by PNR, matches a characteristic domain-wall structure that consists of:

(1) Néel caps at both surfaces: PNR data have shown that at both surfaces, the magnetic SLD was $Np = (0.0 \pm 0.1) \times 10^{-6} \text{ \AA}^{-2}$, which means that no in-plane magnetic moment (parallel to the external applied field) was present. Therefore, this area is mainly formed by out-of-plane (M_z) and in-plane magnetic moments perpendicular to the external applied field (M_y) corresponding to the Néel cap flux-closure structure. The best fittings indicate that this structure had an effective depth of $t_{\text{Néel}} \approx 2.5 \pm 0.6 \text{ nm}$ for the 20-nm-thick film.

(2) A Bloch wall at the center of the film: A constant magnetic SLD of $Np = (0.20 \pm 0.09) \times 10^{-6} \text{ \AA}^{-2}$ ($\approx 18\%$ of the in-plane magnetization saturation value) was obtained at the center of the 20-nm-thick film with a thickness of $t_{\text{Bloch}} \approx 6.2 \pm 0.6 \text{ nm}$.

(3) Intermediate regime: Between these extremes, a region with an average in-plane magnetization of $\approx 10\%$ represented the transition between Bloch wall and Néel caps. This region had an effective thickness of $t_{\text{Néel-Bloch}} \approx 2.0 \pm 0.6 \text{ nm}$ for the 20-nm-thick film.

To simplify the analysis, we therefore approximate the magnetic configuration such that the Néel caps consist of trapezoidal domains with in-plane magnetization and are separated from the out-of-plane domains by 90° walls [30] [see diagram in Fig. 4(d)]. This arrangement provides for the magnetic flux to partially close inside the thin film. At the center of the thin film, adjacent out-of-plane domains are separated by Bloch walls. This model has been well established theoretically [28,29,67,68], and it is in agreement with micromagnetic simulations [69] and results obtained by other experimental techniques, such as CDXRMS [30] and grazing-incidence small-angle scattering (GISANS) [70].

Usually, the Bloch wall width (δ_{Bloch}) can be estimated by the equation [71]

$$\delta_{\text{Bloch}} \approx \pi(A/K_u)^{1/2}, \quad (1)$$

where A ($5 \times 10^{-7} \text{ ergs/cm}$) is the exchange stiffness constant and K_u ($1.225 \times 10^6 \text{ ergs/cm}^3$) is the uniaxial magnetocrystalline anisotropy energy. This yields a Bloch domain-wall width of $\delta_{\text{Bloch}} \approx 20 \text{ nm}$. In comparison, the mi-

cro-magnetic simulations showed that the Bloch domain-wall width extends up to $\approx (25 \pm 5) \text{ nm}$. PNR analysis also provides an effective tool for the determination of δ_{Bloch} . Again, using the approximation that the in-plane magnetic moment of the CoCrPt was mainly localized at the DW, specifically at the Bloch walls, and that these magnetic moments at low fields remained aligned to the direction of the external magnetic field, along the x axis [Fig. 7(b)], δ_{Bloch} can be estimated. PNR data showed that the in-plane magnetization of the CoCrPt layer was $M_x \approx 18\%$ at the center of the layer. In this region of the film, we consider that the magnetic moments were either out-of-plane or in-plane parallel to the field (i.e., the out-of-plane magnetization should correspond to a magnetization of $M_z \approx 82\%$). From the MFM images, the domain width was $\approx 140 \text{ nm}$ at remanence after in-plane saturation. If 82% of magnetization corresponded to 140-nm-wide domains, the 18% in-plane magnetization would correspond to a Bloch wall width of $\delta_{\text{Bloch}} \approx (30 \pm 10) \text{ nm}$, in good agreement with micromagnetic results and with the theoretical width.

Magnetic force microscopy measurements performed by Keitoku *et al.* [72] showed domain sizes of 90–95 nm for 15- and 30-nm-thick $\text{Co}^{0.61}\text{Cr}^{0.13}\text{Pt}^{0.26}$ films, and larger domains of $\approx 250 \text{ nm}$ for 10-nm-thick films. In this case, the domain structures were unaffected by the MFM tip due to high coercivity ($\approx 1 \text{ kOe}$) of the alloy. In our 10-nm-thick CoCrPt film, with coercivity $< 100 \text{ Oe}$, the domain pattern could not be determined by MFM, but we will now show that PNR can yield information about the ferromagnetic domain structure in such samples. Figures 8(a) and 8(b) show the SLDs of the nominally 10-nm-thick CoCrPt layer. Again, the magnetic SLD at low fields decreased to an average value of $Np = (0.06 \pm 0.02) \times 10^{-6} \text{ \AA}^{-2}$, suggesting that only $\approx 5\%$ of the CoCrPt magnetic moment remained aligned with the applied in-plane field guiding the neutron polarization [Fig. 8(c)].

However, nonzero SLD does not necessarily result in spin splitting between NSF reflectivity curves with alternating directions of polarization. Indeed, the observed PNR signal is a result of summation over the total sample surface illuminated by the beam. In reality, the surface is covered with a number of coherence ellipses so that the mean magnetization within each of them may be nonzero, but randomly directed over different coherence ellipses. Then the net magnetization of the sample tends to zero and splitting vanishes. This is just the case for the thin sample, in which the SLD of a magnetic layer in remanence averaged over its thickness dropped by a factor of about two with respect to its value at saturation. At the same time, in the demagnetized sample, the net magnetization was reduced by an additional 92%, which is associated with incoherent averaging over larger domains. This means that demagnetization predominantly occurs via formation of large domains [73] comprising Bloch DWs.

Considering that micromagnetic simulations showed that the DW is a pure Bloch wall for a 10-nm-thick CoCrPt layer [Fig. 4(f)] and assuming that the in-plane magnetic moment along the x axis was exclusively present at the Bloch DWs and that the wall width was equal for the 10- and 20-nm-thick layers, the 5% in-plane magnetization, determined above, corresponded to $\delta_{\text{Bloch}} \approx 30 \pm 10 \text{ nm}$. The out-of-plane magnetization should then correspond to a magnetization value of $M_z \approx 95\%$, and a domain width

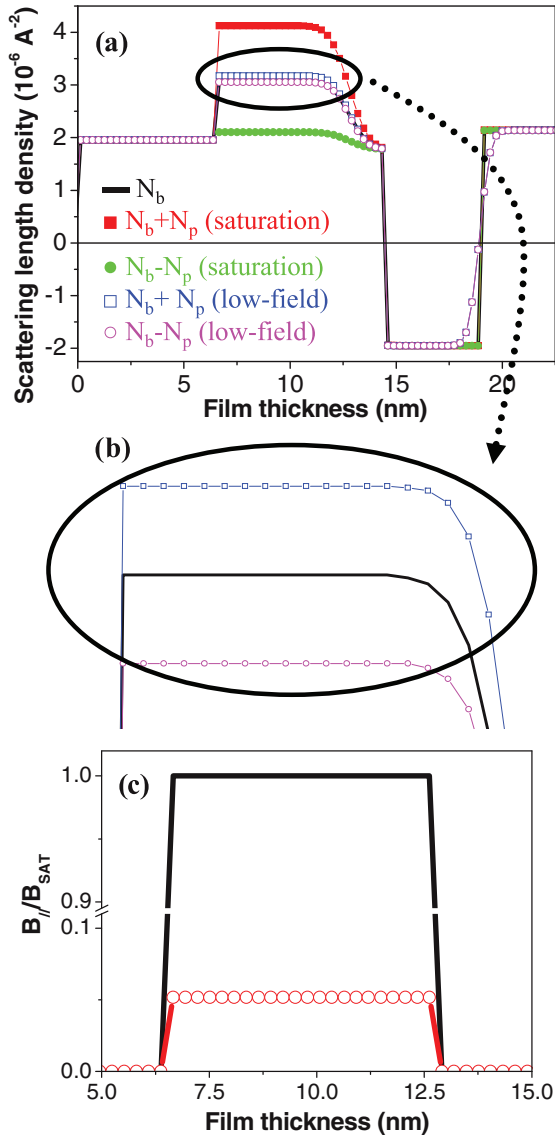


FIG. 8. (Color online) (a) Nuclear SLD (—), (nuclear + magnetic) SLDs in saturation (■) and at low field (□), and (nuclear – magnetic) SLDs in saturation (●) and at low field (○) of the 10-nm-thick CoCrPt film. (b) A magnification of the SLDs, indicated by a circle. (c) Profile of the normalized in-plane magnetization in saturation (—) and at low field (○).

value of $\approx 600 \pm 100$ nm can be estimated. Such enlargement of the magnetic domains with decreasing film thickness was also predicted by our micromagnetic simulations at remanence after in-plane saturation [Fig. 3(e)].

IV. SUMMARY

We have shown that PNR, in combination with MFM and micromagnetic simulations, provides quantitative information about DWs in perpendicular anisotropy films, including their width and through-thickness structure, as well as information about the domain size distribution. A nominally 20-nm-thick CoCrPt film with perpendicular anisotropy contained walls with a Bloch structure at the center of the film with Néel

caps at the surfaces and a transition regime between them. While the Bloch wall was characterized by a width of ≈ 30 nm and in-depth thickness of ≈ 6.2 nm, the Néel caps and the transition regime showed through-thickness dimensions of ≈ 2.5 and 2.0 nm, respectively. On the other hand, a 10-nm-thick film contained walls with a pure Bloch structure. This shows that even thin films can have a complex through-thickness magnetic structure. Polarized neutron reflectivity also provided estimates for domain size and revealed the presence of an intermixed layer at the CoCrPt/Ti interface. Therefore, PNR is a technique for determining the domain size and structure in thin film systems and could be extended to studying the dynamic behavior of thin films [74]. This can provide insight into the development of future devices that involve the behavior, movement, or annihilation of DWs.

ACKNOWLEDGMENTS

D.N. thanks the Ministerio de Economía y Competitividad (MAT2010-20798-C05-02) and Fundação para a Ciência e Tecnologia (Grant No. SFRH/BPD/89808/2012) for financial support and the Institut Laue-Langevin for providing beam time for the PNR experiment and technical support. C.A.R. acknowledges support of C-SPIN, one of six STARnet centers of Microelectronics Advanced Research Corporation (MARCO) and Defense Advanced Research Projects Agency (DARPA).

APPENDIX: DATA TREATMENT FOR PNR ANALYSIS

The magnetic scattering length density (Np) is proportional to the mean value of the magnetization vector projection onto the surface plane (see, e.g., the review article by Zabel *et al.* [34]). In our experiment, an external magnetic field was also applied in the surface plane. Usually, the neutron beam is covering a large area, and in our experiment, it illuminates the whole sample surface. Therefore, the magnetization projection onto the sample surface is averaged over its area. However, it is important to note that there are two types of consequent averaging [34]. The first runs over the volume of the coherence ellipsoid, which is determined by the quantum mechanical uncertainties of incoming and outgoing wave vectors. This uncertainty is related to the instrumental resolution ellipsoid in reciprocal space. In our case, due to grazing incidence, the long axis of the coherence ellipsoid is displayed along the intersection between the surface and the reflection plane and is extended up to $100 \mu\text{m}$ [34,63]. The two short axes are perpendicular to the long axis and amount only up to 10–100 nm. Hence, the area of the intersection between the coherence ellipsoid and the surface is much smaller than the sample area, but the ellipsoid long axis still crosses a number of domains and DWs.

Within the coherence ellipsoid, the result of neutron reflection is described by the complex reflection amplitude R . The measured quantity (i.e., the reflection coefficient $R = \langle |R|^2 \rangle$, or reflectivity) is equal to the modulus squared of the reflection amplitude incoherently averaged over the whole sample surface. Such an averaging is quite trivial in the case when $|R|$ is the same for all different coherence ellipsoids over the sample surface. In the presence of randomness this

is the consequence of the central hypothesis of ergodicity and self-averaging. It allows for easy evaluation of data from laterally inhomogeneous (e.g., multidomain surfaces) and applies when the number of inhomogeneities (domains and DWs) within the coherence volume is sufficiently large. Then specular reflection is due to the mean scattering potential \bar{V} proportional to mean SLD \overline{Nb} averaged over the coherence ellipsoid. Local deviations $V(\vec{r}) - \bar{V}$ from that mean value cause off-specular scattering. If the latter is small, it can be described within the framework of the distorted-wave Born approximation [34,63]. In our experiment, no off-specular scattering was detected: perpendicular domains do not scatter, while DWs are too small. Hence, they scatter into a broad range of angles. At small angles, covered by our position-sensitive detector, scattering from DWs can hardly be distinguished from incoherent background, which is pretty small [75].

Inside magnetic material, neutron spin states are split due to the Zeeman effect, so that there exist two SLDs: $\overline{Nb}^{\pm} = Nb_N \pm \overline{Np}$, where Nb_N is nuclear and Np is magnetic SLD. Correspondingly, there exist two refraction indexes and two reflection amplitudes R^+ and R^- : one for the positive and the other for the negative spin projections onto the mean induction within the coherence range. The averaging for the case of domains separated by a combination of Néel and Bloch walls is sketched in Figs. 4(d) and 4(e). There, due to the continuity of the magnetic flux projection normal to the wall and the requirement of minimum stray field in outer space, magnetization in neighboring “triangular cap domains” must have alternative directions. If so, their contribution to the mean value is canceled after lateral averaging over a large number of domains within the coherence spot. As a result, the mean magnetic SLD in the layers close to the sample surfaces must definitely vanish.

This is not the case for neighboring Bloch walls, in which direction of the magnetic moment is determined by the sense of spins rotation in the walls. Hence, there is no other reason for the alternating of magnetic moments than to avoid a stray field outside the sample. However, in a large sample, the magnetic flux related to Bloch walls can be closed inside the sample at distances larger than the domain size. Over short distances associated with neighboring Bloch DWs, magnetic moments may be antiparallel or parallel to each other or tilted at a certain angle. If, however, the system was previously subjected to a high-magnetic in-plane field, then magnetic moments in neighboring DWs may be still “ferromagnetically” correlated over many neighbors. If the total magnetic flux is closed within the sample surface, then mean magnetization averaged over different coherence ellipsoids should be pointing into different directions. As a result, magnetization averaged over the total sample surface finally turns to zero. Consequently, it cannot be detected in macroscopic measurements but still can be probed with PNR. The situation is similar to that in magnetically soft ferromagnetic films decomposed into a set of large lateral domains. The difference is that now lateral magnetization of domains is provided by Bloch DWs, with which magnetic moments are correlated in a number of neighboring walls but decaying at large distances. Therefore, corresponding large areas carrying mean magnetization can be also called hyperdomains, as was previously observed

[73] in stripe-patterned films. If the number of DWs within hyperdomains is large, then the absolute value (but not direction) of magnetization in each of them is about the same. This means that if the sizes of hyperdomains are comparable to, or greater than, the long axis of the coherence ellipsoid, then amplitudes R^{\pm} are also about the same over the sample surface. This is, again, because the spin splitting, and hence the reflection amplitudes R^+ and R^- are independent of the angle γ between the neutron polarization vector and the direction of hyperdomain induction. In contrast, population factors of neutron spin states are determined by the angle γ .

Indeed, for ideal polarization NSF $R^{\pm\pm}$ and SF $R^{\pm\mp}$ reflection coefficients can be described by the following set of equations [34,63]:

$$\begin{aligned} R^{\pm\pm} &= \frac{1}{2}\{(|R^+|^2 + |R^-|^2) \pm \langle \cos \gamma \rangle (|R^+|^2 - |R^-|^2)\} \\ &\quad - \frac{1}{4}\langle \sin^2 \gamma \rangle |R^+ - R^-|^2 \\ R^{\pm\mp} &= \frac{1}{4}\langle \sin^2 \gamma \rangle |R^+ - R^-|^2. \end{aligned} \quad (\text{A1})$$

Here, the averaging runs over all values of the angle γ in different hyperdomains. Let us note that in the case of alternating magnetic moments within the coherence length, the mean magnetic reflection potential average vanishes. Therefore, $R^+ = R^-$, no SF reflection should be observed, and NSF reflectivities $R^{++} = R^{--}$, while SF $R^{+-} = R^{-+} = 0$. In the opposite limit when all DW moments are parallel but domain magnetization is still perpendicular to the surface, SF specular reflection is also absent. However, $R^{++} = |R^+|^2$, $R^{--} = |R^-|^2$, and $R^{++} \neq R^{--}$ due to the parallel orientation of DW magnetic moments. If the parallel orientation is maintained over a distance greater than the long axis of the coherence ellipsoid, but the sample is decomposed into a set of large (hyper)domains, so that its net magnetization vanishes, then again $R^+ \neq R^-$, but $\langle \cos \gamma \rangle = 0$, and spin splitting $R^{++} - R^{--} = 0$, while both depend on the value of $\langle \sin^2 \gamma \rangle$. The latter, hence SF reflection, may turn to zero, if magnetization of (hyper)domains is with equal probability pointing along with, or opposite to, the polarization vector direction. Still, even though $R^{++} = R^{--}$ and $R^{+-} = R^{-+} = 0$, this situation is quite differs from the first case, when the sample is demagnetized along short distances and reflection amplitudes $R^+ = R^-$ do not contain magnetic SLD. This fact can be determined from, e.g., the position of the critical angle of the total reflection. Finally, one can mention the limiting case of the totally random distribution of magnetization directions averaged over the coherence ellipsoids so that $\langle \cos \gamma \rangle = 0$ and $\langle \sin^2 \gamma \rangle = 1/2$. Then, again, no spin splitting is observed, while strong SF reflection due to $R^{+-} = R^{-+} \neq 0$ is expected.

In our experiment, we observed that the mean $\langle \cos \gamma \rangle$ is about 1/3, and $\langle \sin^2 \gamma \rangle = 0$ in the 10-nm-thick CoCrPt film at low field. The latter means that due to wiggling of DWs, all components perpendicular to the external field are compensated within the coherence ellipsoid. Simultaneously, due to the same wiggling, SLD is reduced down to 18%, while net magnetization down to $(18/3) = 6\%$, in agreement with the hysteresis loops.

From the fact that $\langle \cos \gamma \rangle = 1/3$ and $\langle \sin^2 \gamma \rangle = 0$, it follows that the sample is decomposed into two types of large “hyperdomains” greater than the coherence ellipsoid. While the mean magnetization is looking into the field direction in the first type of hyperdomains, it is pointing opposite the guiding field in the second one.

Let’s introduce the surface fraction x covered with one type of domains with $\gamma_1 = 0^\circ$, and $(1 - x)$ corresponding to

$\gamma_2 = 180^\circ$. Then

$$\begin{aligned} \langle \cos \gamma \rangle &= x \cos(\gamma_1) + (1 - x) \cos(\gamma_2) \\ &= x - (1 - x) = 2x - 1 = 1/3 \end{aligned} \quad (\text{A2})$$

Solving this equation obtains $x = 2/3$. Therefore, the first type of hyperdomain occupies two thirds of the sample area, while the rest is occupied by the second type.

-
- [1] H. J. Richter, *J. Phys. D* **40**, R149 (2007).
 [2] J. H. Judy, *J. Magn. Magn. Mater.* **287**, 16 (2005).
 [3] B. D. Terris and T. Thomson, *J. Phys. D* **38**, R199 (2005).
 [4] C. A. Ross, *Annu. Rev. Mater. Res.* **31**, 203 (2001).
 [5] S. S. P. Parkin, M. Hayashi, and L. Thomas, *Science* **320**, 190 (2008).
 [6] D. A. Allwood, G. Xiong, C. C. Faulkner, D. Atkinson, D. Petit, and R. P. Cowburn, *Science* **309**, 1688 (2005).
 [7] P. Xu, K. Xia, C. Gu, L. Tang, H. Yang, and J. Li, *Nat. Nanotech.* **3**, 97 (2008).
 [8] L. Thomas, M. Hayashi, X. Jiang, R. Moriya, C. Rettner, and S. S. P. Parkin, *Nature* **443**, 197 (2006).
 [9] M. Hayashi, L. Thomas, C. Rettner, R. Moriya, X. Jiang, and S. S. P. Parkin, *Phys. Rev. Lett.* **97**, 207205 (2006).
 [10] M. Laufenberg, W. Bührer, D. Bedau, P.-E. Melchy, M. Kläui, L. Vila, G. Faini, C. A. F. Vaz, J. A. C. Bland, and U. Rüdiger, *Phys. Rev. Lett.* **97**, 046602 (2006).
 [11] E. Martinez, L. Lopez-Diaz, L. Torres, C. Tristan, and O. Alejos, *Phys. Rev. B* **75**, 174409 (2007).
 [12] D. Ravelosona, D. Lacour, J. A. Katine, B. D. Terris, and C. Chappert, *Phys. Rev. Lett.* **95**, 117203 (2005).
 [13] S. W. Jung, W. Kim, T. D. Lee, K. J. Lee, and H. W. Lee, *Appl. Phys. Lett.* **92**, 202508 (2008).
 [14] H. Tanigawa, T. Koyama, G. Yamada, D. Chiba, S. Kasai, S. Fukami, T. Suzuki, N. Ohshima, N. Ishiwata, Y. Nakatani, and T. Ono, *Appl. Phys. Express* **2**, 053002 (2009).
 [15] E. Martinez, L. Lopez-Diaz, O. Alejos, and L. Torres, *J. Appl. Phys.* **106**, 043914 (2009).
 [16] I. M. Miron, T. Moore, H. Szabolcs, L. D. Buda-Prejbeanu, S. Auffret, B. Rodmacq, S. Pizzini, J. Vogel, M. Bonfim, A. Schuhl, and G. Gaudin, *Nat. Mater.* **10**, 419 (2011).
 [17] K.-S. Ryu, L. Thomas, S.-H. Yang, and S. Parkin, *Nat. Nanotech.* **8**, 527 (2013).
 [18] S. Emori, U. Bauer, S.-M. Ahn, E. Martinez, and G. S. D. Beach, *Nat. Mater.* **12**, 611 (2013).
 [19] N. L. Schryer and L. R. Walker, *J. Appl. Phys.* **45**, 5406 (1974).
 [20] A. Mougin, M. Cormier, J. P. Adam, P. J. Metaxas, and J. Ferre, *Europhys. Lett.* **78**, 57007 (2007).
 [21] J. M. Garcia, A. Thiaville, J. Miltat, K. J. Kirk, J. N. Chapman, and F. Alouges, *Appl. Phys. Lett.* **79**, 656 (2001).
 [22] A. Berger and H. P. Oepen, *Phys. Rev. B* **45**, 12596 (1992).
 [23] M. Laufenberg, D. Backes, W. Bührer, D. Bedau, M. Kläui, U. Rüdiger, C. A. F. Vaz, J. A. C. Bland, L. J. Heyderman, F. Nolting, S. Cherifi, A. Locatelli, R. Belkhou, S. Heun, and E. Bauer, *Appl. Phys. Lett.* **88**, 052507 (2006).
 [24] T. A. Duckworth, F. Ogrin, S. S. Dhesi, S. Langridge, A. Whiteside, T. Moore, G. Beutier, and G. van der Laan, *Optic Express* **19**, 16223 (2011).
 [25] P. R. Aitchison, J. N. Chapman, V. Gehanno, I. S. Weir, M. R. Scheinfein, S. McVitie, and A. Marty, *J. Magn. Magn. Mater.* **223**, 138 (2001).
 [26] A. Bellec, S. Rohart, M. Labrune, J. Miltat, and A. Thiaville, *Europhys. Lett.* **91**, 17009 (2010).
 [27] H. F. Ding, W. Wulfhekel, and J. Kirschner, *Europhys. Lett.* **57**, 100 (2002).
 [28] C. Kittel, *Phys. Rev.* **70**, 965 (1946).
 [29] A. Hubert and R. Schafer, *Magnetic Domains: The Analysis of Magnetic Microstructures* (Springer, New York, 1998).
 [30] H. A. Dürr, E. Dudzik, S. S. Dhesi, J. B. Goedkoop, G. van der Laan, M. Belakhovsky, C. Mocuta, A. Marty, and Y. Samson, *Science* **284**, 2166 (1999).
 [31] H. Zabel, *Physica B* **198**, 156 (1994).
 [32] G. P. Felcher, S. Adenwalla, V. O. De Haan, and A. A. Van Well, *Nature (London)* **377**, 409 (1995).
 [33] H. Zabel, *Mater. Today* **9**, 42 (2006).
 [34] H. Zabel, K. Theis-Bröhl, and B. P. Toperverg, in *Handbook of Magnetism and Advanced Magnetic Materials*, edited by H. Kronmüller and S. Parkin (Wiley, New York, 2007), p. 1237.
 [35] Y. Matsuda, Y. Yahisa, J. Inagaki, and A. Ishikawa, *J. Appl. Phys.* **79**, 5351 (1996).
 [36] M.-Y. Im, P. Fischer, D.-H. Kim, K.-D. Lee, S.-H. Lee, and S.-C. Shin, *Adv. Mater.* **20**, 1750 (2008).
 [37] M. Futamoto, Y. Honda, H. Kakibayashi, and K. Yoshida, *IEEE Trans. Magn.* **21**, 1426 (1985).
 [38] Y. Sonobe, Y. Ikeda, H. Uchida, and T. Toyooka, *J. Appl. Phys.* **81**, 4667 (1997).
 [39] F. Ilievski, C. A. Ross, and G. J. Vancso, *J. Appl. Phys.* **103**, 07C520 (2008).
 [40] www.ill.eu/instruments-support/instruments-groups/instruments/superadam/
 [41] M. J. Donahue and D. G. Porter, *OOMMF User’s Guide, Version 1.0*, National Institute of Standards and Technology Report No. NISTIR 6376, 1999.
 [42] C. L. Platt, K. W. Wierman, E. B. Svedberg, T. J. Klemmer, J. K. Howard, and D. J. Smith, *J. Magn. Magn. Mater.* **247**, 153 (2002).
 [43] G. M. Chow, C. J. Sun, E. W. Soo, J. P. Wang, H. H. Lee, D. Y. Noh, T. S. Cho, J. H. Je, and Y. K. Hwu, *Appl. Phys. Lett.* **80**, 1607 (2002).
 [44] M. Futamoto, K. Terayama, K. Sato, and Y. Hirayama, *Scr. Mater.* **48**, 929 (2003).
 [45] M.-Y. Im, D.-H. Kim, and S.-C. Shin, *Phys. Rev. B* **72**, 132416 (2005).
 [46] N. Inaba, Y. Uesaka, and M. Futamoto, *IEEE Trans. Magn.* **36**, 54 (2000).

- [47] H. Y. Sun, J. Hu, Z. F. Su, J. L. Xu, and S. Z. Feng, *IEEE Trans. Magn.* **42**, 1782 (2006).
- [48] J. E. Davies, O. Hellwig, E. E. Fullerton, G. Denbeaux, J. B. Kortright, and K. Liu, *Phys. Rev. B* **70**, 224434 (2004).
- [49] Free software at <http://www.nanotec.es>. A description of the software performance can be found in I. Horcas, R. Fernandez, J. M. Gomez-Rodriguez, J. Colchero, J. Gomez-Herrero, and A. M. Baro, *Rev. Sci. Instrum.* **78**, 013705 (2007).
- [50] D. Navas, C. Nam, D. Velazquez, and C. A. Ross, *Phys. Rev. B* **81**, 224439 (2010).
- [51] N. Inaba and M. Futamoto, *J. Appl. Phys.* **87**, 6863 (2000).
- [52] S. Saito, N. Itagaki, and M. Takahashi, *IEEE Trans. Magn.* **40**, 2467 (2004).
- [53] J. W. Lau, R. D. McMichael, and M. J. Donahue, *J. Res. Natl. Inst. Stand. Technol.* **114**, 57 (2009).
- [54] K. Piao, D. J. Li, and D. Wei, *J. Magn. Magn. Mater.* **303**, e39 (2006).
- [55] P. Krone, M. Albrecht, and T. Schrefl, *J. Magn. Magn. Mater.* **323**, 432 (2011).
- [56] M. Igarashi, M. Hara, A. Nakamura, and Y. Sugita, *IEEE Trans. Magn.* **39**, 1897 (2003).
- [57] N. Honda, T. Kiya, J. Ariake, K. Ouchi, and S. Iwasaki, *IEEE Trans. Magn.* **38**, 2030 (2002).
- [58] J.-G. Zhu, H. Yuan, S. Park, T. Nuhfer, and D. E. Laughlin, *IEEE Trans. Magn.* **45**, 911 (2009).
- [59] W. Wang, C. Mu, B. Zhang, Q. Liu, J. Wang, and D. Xue, *Comput. Mater. Sci.* **49**, 84 (2010).
- [60] J. M. Shaw, S. E. Russek, T. Thomson, M. J. Donahue, B. D. Terris, O. Hellwig, E. Dobisz, and M. L. Schneider, *Phys. Rev. B* **78**, 024414 (2008).
- [61] F. Ilievski, A. Cuchillo, W. Nunes, M. Knobel, C. A. Ross, and P. Vargas, *Appl. Phys. Lett.* **95**, 202503 (2009).
- [62] D. Navas, F. Ilievski, and C. A. Ross, *J. Appl. Phys.* **105**, 113921 (2009).
- [63] B. P. Toperverg, in *Polarized Neutron Scattering*, Jülich Series Matter, and Materials, edited by Th. Brückel and W. Schweika (Forschungszentrum Jülich GmbH, Institut für Festkörperforschung, Jülich, Germany, 2002), Vol. 12, p. 249.
- [64] S. Saito, F. Hoshi, and M. Takahashi, *J. Appl. Phys.* **91**, 8028 (2002).
- [65] M. Futamoto, Y. Hirayama, Y. Honda, and N. Inaba, *J. Magn. Magn. Mater.* **226–230**, 1610 (2001).
- [66] L. D. Landau and E. M. Lifshitz, *Course of Theoretical Physics, Theory of the Condensed State* (Pergamon, Oxford, 1980), Vol. IX, Part 2.
- [67] L. D. Landau and E. Lifshitz, *Phys. Z. Sowjetunion* **8**, 153 (1935).
- [68] A. P. Malozemoff and J. C. Slonczewski, *Magnetic Domain Walls in Bubble Materials* (Academic Press, New York, 1979).
- [69] M. Viret, Y. Samson, P. Warin, A. Marty, F. Ott, E. Søndergård, O. Klein, and C. Fermon, *Phys. Rev. Lett.* **85**, 3962 (2000).
- [70] M. Pannetier, F. Ott, C. Fermon, and Y. Samson, *Physica B* **335**, 54 (2003).
- [71] R. C. O’Handley, *Modern Magnetic Materials: Principles and Applications* (Wiley, New York, 2000).
- [72] T. Keitoku, J. Ariake, N. Honda, and K. Ouchi, *J. Magn. Magn. Mater.* **235**, 34 (2001).
- [73] K. Theis-Bröhl, A. Westphalen, H. Zabel, U. Rücker, J. McCord, V. Höink, J. Schmalhorst, G. Reiss, T. Weis, D. Engel, A. Ehresmann, and B. P. Toperverg, *New J. Phys.* **10**, 093021 (2008).
- [74] K. Zhernenkov, D. Gorkov, B. P. Toperverg, and H. Zabel, *Phys. Rev. B* **88**, 020401(R) (2013).
- [75] A. Devishvili, K. Zhernenkov, A. J. C. Dennison, B. P. Toperverg, M. Wolff, B. Hjörvarsson, and H. Zabel, *Rev. Sci. Instrum.* **84**, 025112 (2013).